MASARYKOVA UNIVERZITA
Přírodovědecká fakulta
Ústav teoretické fyziky a astrofyziky

BAKALÁŘSKÁ PRÁCE

Zpracování dat z interferometru ALMA – vývoj galaktických medúz v kupě Coma

Jakub Gazdoš

Vedoucí práce: Mgr. Pavel Jáchym, Ph.D.

Brno 2023

Bibliografický záznam:

Autor:	Jakub Gazdoš Přírodovědecká fakulta, Masarykova univerzita Ústav teoretické fyziky a astrofyziky
Název práce:	Zpracování dat z interferometru ALMA – vývoj galaktických medúz v kupě Coma
Studijní program:	B-FYZ Fyzika
Studijní obor:	Astrofyzika
Vedoucí práce:	Mgr. Pavel Jáchym Ph.D.
Akademický rok:	2022/2023
Počet stran:	vi + 37
Klíčová slova:	galaxie: kupy: konkrétní (Vlasy Bereniky) – galaxie: vývoj – galaxie: konkrétní (D100, GMP2374) – galaxie: mezihvězdná látka – galaxie: hvězdotvorba – radiové spektrální čáry: mezihvězdná látka – technika: interferometrie

Bibliographic Entry:

Author:	Jakub Gazdoš Faculty of Science, Masaryk University Department of physics and astrophysics
Thesis Title:	Processing of Interferometry ALMA Data - Evolution of Jellyfish Galaxies in the Coma Cluster
Degree Programme:	B-FYZ Physics
Field of Study:	Astrophysics
Supervisors:	Mgr. Pavel Jáchym Ph.D.
Academic Year:	2022/2023
Number of Pages:	vi + 37
Keywords:	galaxies: clusters: individual (Coma) — galaxies: evolution — galaxies: individual (D100, GMP2374) — galaxies: ISM — galaxies: star formation — radio lines: ISM – techniques: interferometric

Abstrakt

Tato práce se zabývá zpracováním a zobrazením radio-interferometrických dat z dalekohledu Atacama Large Millimeter/submillimeter Array (ALMA). Pozorovali jsme dvě galaxie, značené D100 a GMP2374 (NGC4911), nacházející se v galaktické kupě v souhvězdí Vlasy Bereniky. U obou bylo již dříve pozorováno, ve viditelném oboru a ve spektrální čáře Hα, že jejich hmota byla narušena dynamickým působením hustého prostředí kupy. ALMA pozorovala na spektrální čáře CO rotačního přechodu J 2 –> 1, která se používá jako nepřímý indikátor molekulární vodíku. Naše pozorování našlo shodu v distribuci molekulárního plynu s předchozím pozorováním; galaxie D100 se nachází v pokročilém stádiu strhávání hmoty, zatímco u galaxie GMP2374 je tento efekt mnohem méně výrazný. Porovnali jsme důsledky interakce s okolní látkou u pozorovaných galaxií a uvedli možné příčiny odlišností. Na závěr jsme z měření odhadli hmotnost molekulární komponenty galaxií a spočetli odhady současného dynamického tlaku okolního prostředí a jeho maximální hodnotu, kterou kdy galaxie v minulosti zakusily.

Abstract

This work focuses on the processing and imaging of radio-interferometric data from the Atacama Large Millimeter/submillimeter Array (ALMA). We observed two galaxies, the D100 and the GMP2374 (NGC4911), both located in the Coma cluster. Both were previously observed, in the visible light and the Hα spectral line, to have their matter perturbed by the rich environment of the cluster. We observed them at the CO(2-1) rotational spectral line, which is used as an indirect tracer of molecular hydrogen. Our observations found the distribution of the molecular component agrees with the previous observations; the D100 is in an advanced stage of the stripping, while in the GMP2374 the effect is far less pronounced. We compared the impact of the ram pressure stripping process between the two galaxies and presented probable reasons causing the difference. Lastly, estimates of the molecular mass were calculated from our measurements, as well as estimates of the pressure the galaxies are enduring now, and of the maximum pressure they have experienced in the past.

MUNI
SCI

MASARYKOVA UNIVERZITA
PŘÍRODOVĚDECKÁ FAKULTA
KOTLÁŘSKÁ 2, 611 37 BRNO
IČ: 00216224
DIČ: CZ00216224

ZADÁNÍ
BAKALÁŘSKÉ PRÁCE

Akademický rok: 2022/2023

Ústav:	Ústav teoretické fyziky a astrofyziky
Student:	Jakub Gazdoš
Program:	Fyzika
Specializace:	Astrofyzika

Ředitel *ústavu* PřF MU Vám ve smyslu Studijního a zkušebního řádu MU určuje bakalářskou práci s názvem:

Název práce:	Zpracování dat z interferometru ALMA - vývoj galaktických medúz v kupě Coma
Název práce anglicky:	Processing of interferometry ALMA data - evolution of jellyfish galaxies in the Coma cluster
Jazyk závěrečné práce:	angličtina

Oficiální zadání:
Interferometr ALMA je špičkové zařízení pro astronomický výzkum v moderním (sub-)milimetrovém oboru. V rámci projektu mapování CO záření chladného molekulárního plynu se zaměřil na galaxie v blízké kupě galaxií Coma (v souhvězdí Vlasů Bereniky). Tyto tzv. galaktické medúzy (jellyfish galaxies) procházejí silným vývojem v důsledku dynamické interakce s okolním mezigalaktickým plynem. Jak se galaxie přibližují po svých drahách k centru kupy, dynamický tlak okolního prostředí roste a dokáže z galaxií odstranit jejich mezihvězdnou hmotu. Tím dochází k zastavení tvorby nových hvězd a galaxie se mění v pasivní rané typy. Odtržený materiál vytváří u galaxií jednostranné struktury, jakési „kometární ohony“, v nichž se galaktický plyn míchá s mezigalaktickým plynem a vytváří se vícesložkové prostředí. Navrhovaná práce se zaměří na seznámení se s metodami kalibrace a zobrazení interferometrických dat a jejich praktickou aplikaci na ALMA pozorování dvou galaxií v kupě Coma: NGC 4911 a D100. Tyto galaxie se výrazně liší svou morfologií v záření Halpha čáry ionizovaného plynu: jedna je v rané fázi interakce, kdy plynný disk galaxie je jen mírně porušený, zatímco druhá je již v pokročilé fázi, jak nasvědčuje její silně omezený plynný disk a přítomnost dlouhého ohonu. Očekávaným výsledkem práce je vytvoření „vyčištěné“ datové kostky pro obě galaxie pomocí SW CASA a studium hlavních rysů rozložení jejich molekulárního plynu, jako měření poloměru molekulárního disku, rozsahu ohonu, měření gradientů rychlosti atp. Tyto dvě galaxie budou porovnány z pohledu svých rozdílných fází interakce s okolním plynem v kupě Coma.

Vedoucí práce:	Mgr. Pavel Jáchym, Ph.D.
Datum zadání práce:	23. 11. 2022
V Brně dne:	17. 5. 2023

Zadání bylo schváleno prostřednictvím IS MU.

Jakub Gazdoš, 24. 11. 2022
Mgr. Pavel Jáchym, Ph.D., 1. 12. 2022
RNDr. Luboš Poláček, 8. 12. 2022

Poděkování

Děkuji svému vedoucímu práce Pavlu Jáchymovi a své konzultantce Romaně Grossové. Děkuji za pomoc při seznamování s programy na zpracování dat. Děkuji za pomoc s výpočty a hledáním vhodných zdrojů. Děkuji za pomoc při interpretaci výsledků. Děkuji za pomoc při korekci práce.

Děkuji svým přátelům za rady a podporu duševního klidu.

Své rodině děkuji za veškerou jejich podporu.

Prohlášení

Prohlašuji, že jsem svoji bakalářskou práci vypracoval samostatně pod vedením vedoucího práce s využitím informačních zdrojů, které jsou v práci citovány.

V Brně 23. května 2023

_____

Jakub Gazdoš

Contents

Introduction

In this work we process interferometric data from the Atacama Large Millimeter/submillimeter Array, the state-of-the-art instrument in modern radio astronomy. Our goal was to map the distribution of the molecular gas component in two galaxies in the Coma cluster. The stellar disk, dust extinction, and warm ionized component of the galaxies D100 and GMP2374 (NGC4911) were previously observed in the visible light, by the Hubble Space Telescope and the Subaru telescope, to be affected by the interaction with the surrounding intra-cluster matter. We aim to bring insight on how the molecular gas component is impacted by the ram pressure stripping, which reduces the formation of new stars in the galaxy and plays a major role in the galaxy evolution in the rich environment of galaxy clusters. We also try to estimate which stage of the RPS process the galaxies find themselves in, supported by calculations made from the physical properties of the galaxies and the surrounding matter.

First we look at the basics of radio astronomy and how radio interferometry allows us to delve into the depths of the distant space. The second section describes what are galaxies and what kind of matter they contain. We continue with the classification of galaxies and their basic morphology. After that we describe the structure of galaxy clusters and how galaxies respond to the rich environment, focusing on the process of ram pressure stripping. The third section introduces the targets of our observations, the galaxies D100 and GMP2374 located in the Coma cluster, and the method used for observing the molecular gas. The fourth section describes the structure and parameters of the dataset, calibration methods, the calibration pipeline and the process of cleaning the interferometric data to produce an image. This section ends with the products of further processing of the cleaned image, moment maps and position-velocity diagrams. In the last section we summarize the results and compare them to estimates calculated from the physical properties of the galaxies and the cluster.

Section 1:

Radio Astronomy

Written with the information from Marr, Snell, and Kurtz (2015), Cortes et al. (2023).

In comparison to optical astronomy and astrometry, radio astronomy is a much younger discipline. While some experiments detecting extra-terrestrial radio signal had been attempted as early as 1880s, the first successful one is widely accepted to be by Karl Jansky in 1932.

1.1 Electromagnetic Radiation

By developing his electromagnetic equations in the 19th century, J. C. Maxwell managed to describe light as a wave in the electromagnetic field. Furthermore, his theory indicated that visible light occupies only a fraction of the electromagnetic spectrum, as foretold by the discovery of infrared radiation at the dawn of the century.

Electromagnetic waves come in a continuous spectrum of wavelengths. Based on their wavelength, they exhibit different properties. While not showing any exact boundaries, the spectrum has been split into several parts. However, they all propagate through vacuum at the speed of light $c = 3 \times 10^8\,\mathrm{m\,s^{-1}}$, regardless of their wavelength. EM waves can also be described by their frequency. For a simple wave with a single frequency, the wavelength λ, frequency ν and speed c are tied through the formula $\lambda\,\nu = c$.

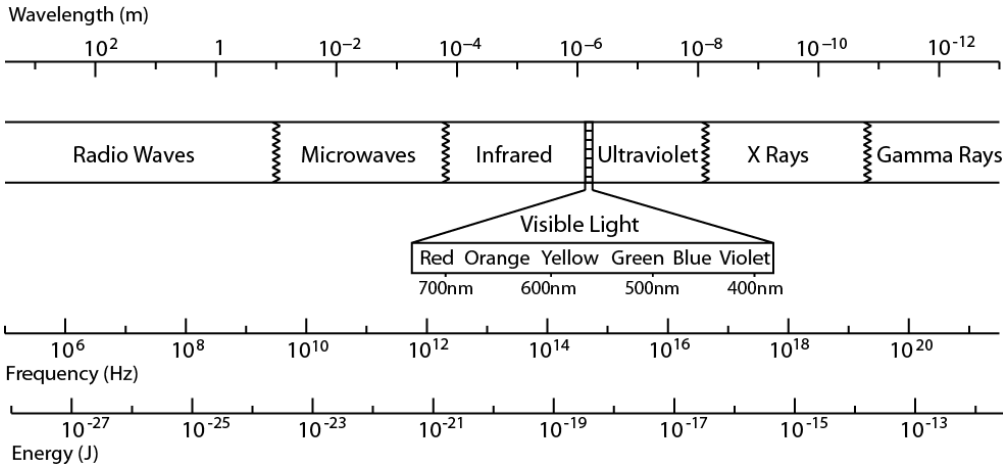

Figure 1: Classification of the EM spectrum based on the wavelength. Also shown is the corresponding frequency and energy. From Marr, Snell, and Kurtz (2015).

1.2 Radio Waves

At the long-wavelengh part of the spectrum lie the microwaves and the radio waves. Gases and particles in Earth's atmosphere interact with EM waves coming from space. While helpful at keeping us alive by blocking dangerous radiation, this limits our ability to study the outside universe. Thankfully, besides visible light it allows certain wavelengths of microwaves and radiowaves to pass through. This is known as the "radio window", spanning from 30 meters (10 MHz) to 1 mm (300 GHz).

Longer waves get absorbed or reflected by free electrons in the ionosphere, while shorter waves are absorbed by H_2O and O_2 molecules. Unfortunately, this makes ground-based observations of such molecules difficult. Either we have to observe at high altitudes and dry places such as mountain tops or completely avoid the atmosphere by using space-based radio telescopes.

Radio waves possess the ability to interfere. When two waves meet they interact. When their amplitudes align, they are in phase, they add up and create a stronger wave. We call this constructive interference. When they do not align, they are out of phase, they subtract and create a weaker wave. We call that destructive interference.

Multiple waves of different orientation and frequencies can interact in such a manner. Coherence expresses the similarity of these properties. Waves coming from the same direction are spatially coherent. When coming from different directions the wave fronts are not parallel and the resulting wave changes with position. Waves of various frequencies shift phase with each other in time and thus the interference changes with time, reducing temporal coherence.

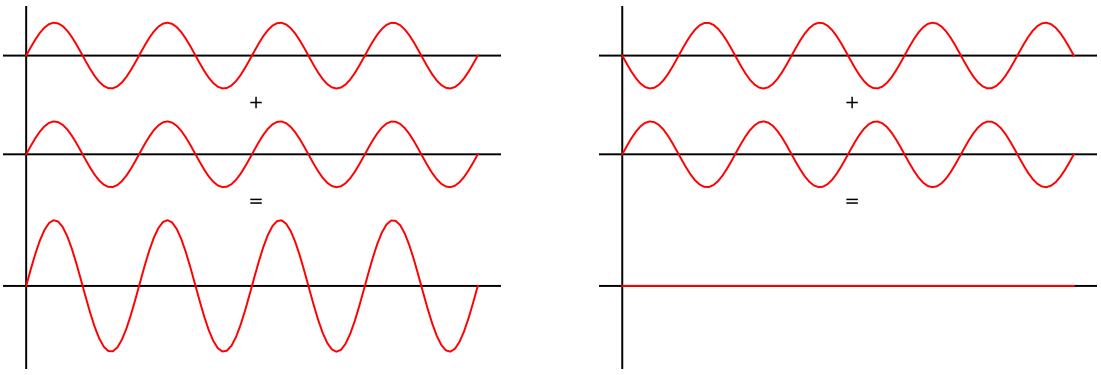

Figure 2: Illustration of the interference of waves with the same wavelength, left: constructive interference, right: destructive interference

1.3 Radio Telescopes

Similar to light, radio waves are reflected off surfaces. A reflector, commonly called a dish, is used to focus incoming waves into the antenna that transforms them into electrical signal. The bigger the area of the dish, the more radiation it collects and enables us to detect fainter objects. The reflector also provides directivity, the ability to differentiate between emission from two close sources. Directivity of a radio telescope is described by the beam pattern.

The beam pattern describes the sensitivity of a telescope as a function of the angle from the axis of the reflector. Imagine a distant point source located at the axis and consider only signal reflected on two points on the reflector the same distance from the axis. Since the wave is perpendicular to the reflector plane, the path lengths of the signal coming from the two points are equal. This means the waves are in phase and we get constructive interference.

If we move the point source away from the axis of the dish, the path lengths from the two symmetric points start to differ. The waves get out of phase and the resulting wave gets weaker. The sensitivity falls until the waves are exactly out of phase and we get no signal. Increasing the angle further shifts the phase and increases the sensitivity again. Though, when we take into account the whole surface of the dish, the secondary peaks are much weaker than the main on-axis peak. These secondary peaks are commonly called sidelobes and are inconvenient as they distort the measurements.

The central peak of the beam pattern is called the main beam. Its width defines the angular resolution of the telescope. The width is determined as the width between the two points where the value equals half the maximum, thus the name full width at half maximum – FWHM. When two sources are spaced closely than the FWHM of the telescope, they are detected as one. It can be calculated from the wavelength λ and diameter of the dish D, giving us the angular resolution of the telescope

$$\Theta = 1.02 \frac{\lambda}{D}. \tag{1}$$

If we wanted to observe at 1mm wavelength and achieve an angular resolution of $1''$, according to this formula we would need a dish with a diameter of 210 meters. Constructing such a telescope would be complicated. Luckily, it is not required for the telescope to have a single dish. The solution to this problem is presented in the next subsection.

Because the response to the signal is not uniform across the main beam we have to correct the resulting image. The process compensating for the decreasing antenna power response is called the primary beam correction. It allows us to get accurate measurements of intensities and flux densities at the edges of the image. For extended emission the telescope can not contain the whole object in

one pointing of the antenna. For such emission we have to make a mosaic with a series of pointings. In a mosaic neighbouring pointings typically overlap and make a complex beam pattern. In this case primary beam correction is crucial for taking accurate measurements.

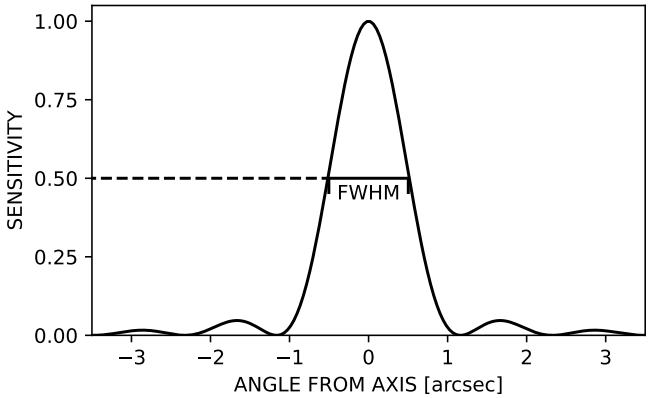

Figure 3: Illustration of the beam pattern, marked FWHM of 1 arcsec

1.4 Aperture synthesis

Aperture synthesis is the process of combining measurements from multiple antennas. Just as waves interfere with each other, signals from two antennas can be combined and produce a better picture of the observed object. Such a pair of antennas is then called an interferometer. We use the term baseline to describe the distance between the two antennas.

By laying out a number of antennas and using each pair as an interferometer we can simulate a large telescope. It provides the resolution of a single dish telescope with the diameter roughly equal to the largest baseline in the array. However, the total collected signal is proportional to the total collecting area and since the sum of the areas of the individual antennas is smaller than that of a singular dish with the corresponding diameter, the total sensitivity is also much weaker.

An important effect of using interferometry is that the sensitivity to extended sources decreases with increasing baseline. Choosing the baseline is thus a trade-off between angular resolution and the ability to detect diffuse emission. Because of this, arrays have configurable antenna positioning to allow different baselines. For point sources the antennas are spaced out to offer the best resolution. On the other hand, measuring extended sources requires the antennas close together.

Because a source is not always positioned in the axis of the interferometer, referred to as the phase center, there exists a phase difference between each pair of

antennas. Due to Earth's rotation the phase difference also changes over time. This effect is predictable and easily corrected. The rotation of the Earth is also helpful during observations as it changes the effective baseline of the interferometer, which improves the sampling in the complex visibility plane, explained in Section 4.2.

1.5 The Atacama Large Millimeter/submillimeter Array

An example of such a telescope is the Atacama Large Millimeter/submillimeter Array (ALMA). It is located on the Chajnantor plain in Chile. An elevation of 5000 m ensures a stable dry atmosphere, that is essential for observing at short radio wavelengths. It covers a range of wavelengths from 0.32 mm to 8.5 mm.

To provide a versatile observing tool the array has two sets of antennas. The 12-m Array has fifty 12m diameter antennas. They can be positioned in various configurations with baselines stretching up to 16 km. This array is used for precise, high-resolution measurements. The other set, the Atacama Compact Array (ACA), is composed of four 12m antennas and twelve 7m antennas. These antennas are closely spaced and are used for the imaging of extended sources.

Figure 4: Picture of the antennas of the Atacama Large Millimeter/submillimeter Array. Credit: ESO/C. Malin (christophmalin.com)

Section 2:

Galaxies

Written with the information from Hubble (1937), Cortese, Catinella, and Smith (2021), Boselli, Fossati, and Sun (2022).

Galaxies are the oases of the vast space, hosting millions of stars. They store an enormous amount of gas and dust, called the interstellar medium (ISM), from which new stars arise and bring light to the dark sky. One of the main components of the ISM is molecular hydrogen H_2, concentrated in cold dense molecular clouds. Neutral HI and ionized HII are found in thinner nebulae. The overall density of matter is highest in the center and falls with the distance.

The first classification of galaxies was presented by Edwin Hubble in 1926 and is commonly used to this day, illustrated in Figure 5. It emerges from the visual shape of the galaxy, referred to as visual morphology. First, he split them into groups based on their symmetry with respect to the galaxy center, as regular or irregular galaxies. Regular galaxies are further divided into ellipticals, lenticulars and spirals.

Elliptical galaxies look round and featureless. They are marked with the letter E and a number referring to their eccentricity from 0 (spherical) to 9 (most eccentric). Spirals have distinct disk-like structure. Most of their matter is concentrated in the galactic disk. There we observe galactic arms, areas of higher ISM density. The increased matter density causes the formation of new stars. The galaxy center is surrounded by the galactic bulge, a dense cloud of matter. Some spirals have a bar in the center connecting the galactic arms, leading to their name barred spirals. We mark them with the letter S, with B added in the case of barred spirals, and a range of letters from a to c representing the shape of the arms. Lenticular galaxies are a middle-link between ellipticals and spirals, marked as S0. Their matter is shaped into a disk, but does not form any arms.

The S0-type galaxies are highly relevant for this work since ram pressure stripping of the ISM from cluster galaxies, followed by the quenching of star formation is believed to be one of the main agents for galaxy evolution from the blue star-forming types to the red quiescent types, through the so-called green valley (see Figure 6).

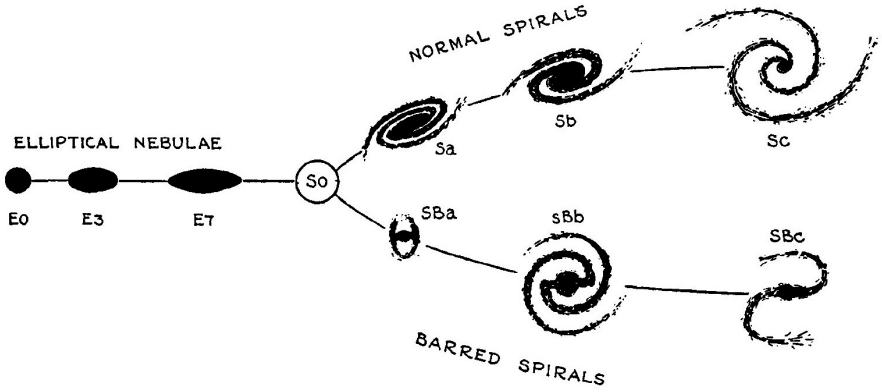

Figure 5: Classification of galaxies, known as the Hubble sequence. The term elliptical nebulae comes from the historical fact that at the time of its creation, galaxies were thought to be nebulae. Taken from Hubble (1937).

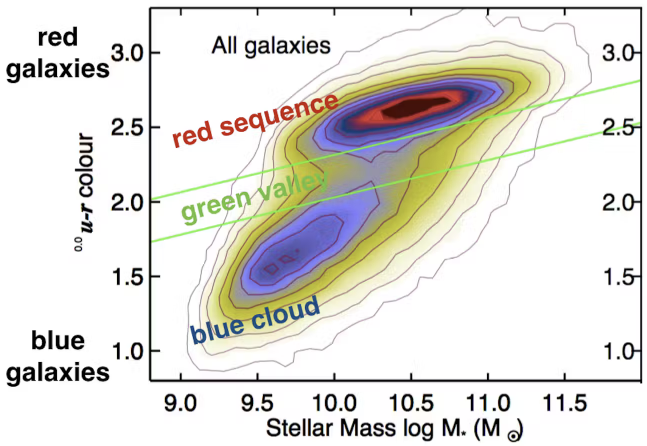

Figure 6: The galaxy color-mass diagram. Blue, star-forming galaxies are in the bottom blue cloud, red, quiescent galaxies are at top red sequence, with the transition zone of the green valley region in between. From Schawinski et al. (2014).

2.1 Galaxy clusters

Approximately 10 % of galaxies are located in galaxy clusters. A cluster contains hundreds to thousands of galaxies. The space between galaxies is filled with hot, X-ray emitting gas, known as the intracluster medium (ICM). It accounts for a significant fraction of the visible mass, often exceeding the galactic mass. But most of the mass comes from dark matter, that holds the cluster together by its gravitational pull. Clusters are found at the clumps of the web-like structure of dark matter.

The morphological composition of galaxies in clusters differs from galaxies in the free field. They tend to be dominated by elliptical (E) and lenticular (S0) galaxies. Galaxies in clusters often exhibit HI and H_2 gas deficiency, that is tied to a decline in the formation of stars in the galaxy. They also show signs of asymmetry of their gas content, sometimes evidently visible in the form of a so called tail. These irregularities are explained by several mechanisms contributed to the influence of the surrounding matter.

The first are gravitational mechanisms. They are tied by their origin in the gravitational force. The tremendous mass of the cluster disturbs the gravitational potential of the galaxy and allows the gas to escape into the surrounding space. We talk of galaxy-cluster interaction. However, if two galaxies come close enough, they can also cause a mutual gravitational disturbance. In this case we talk of galaxy-galaxy interaction. A galaxy can experience multiple g-g interactions during its lifetime, a phenomenon referred to as galaxy harassment.

Second we recognize hydro-dynamical mechanisms. They originate from direct contact between the ICM and the ISM and are tied to the motion of the galaxy through the cluster. In a process called ram pressure stripping, the ICM in the way of the galaxy exerts pressure on the galaxy that strips it of its gas. Gas can also get removed by viscous momentum transfer at the outer layers, then we talk of viscous stripping. Thermal evaporation occurs due to the temperature difference of the gas regions. The cold ISM warms up at the interface with the hot ICM, evaporates and expands out of the galaxy.

These mechanisms rarely act alone. A galaxy experiences different combinations of them during its orbit in the cluster. This makes measuring their ratio and studying their effects somewhat complicated. However, while the gravitational mechanisms affect all forms of matter, the direct-contact mechanisms affect only the diffuse gas component. Another difference is that the effects of gravitational influence are oriented in the direction of the cluster center, in the case of g-c interactions, or the foreign galaxy in g-g interactions. On the other side, hydro-dynamical effects are directed opposite to the galaxy movement.

2.2 Ram Pressure Stripping (RPS)

A galaxy orbiting through the cluster pushes against the hot dense gas in front. This applies a drag force on the diffuse ISM of the galaxy. According to Gunn and Gott (1972), when the drag force overcomes the restoring force caused by the gravitational influence of the galaxy

$$\rho_{\mathrm{ICM}}\, v_{\mathrm{gal}}^2 \geq \left.\frac{\partial \Phi(r,z)}{\partial z}\right|_{max} \Sigma_{\mathrm{gas}}, \tag{2}$$

the diffuse gas is shoved out of the galaxy. ρ_{ICM} is the density of the ICM, v_{gal} the velocity of the galaxy relative to the cluster, $\Phi(r,z)$ the total gravitational potential of the galaxy as a function of the galactocentric cylindrical coordinates and Σ_{gas} the surface density of the gas component.The inequality 2 can be also expressed using observable quantities:

$$\rho_{\mathrm{ICM}}\, v_{\mathrm{gal}}^2 \geq 2\pi\, G\, \Sigma_{\mathrm{star}}\, \Sigma_{\mathrm{gas}}, \tag{3}$$

where G is the gravitational constant and Σ_{star} the surface density of the stellar component.

Thinner gas such as HI and HII is more susceptible to stripping than H_2 gas, which is denser and commonly hidden in molecular clouds. The process acts outside-in meaning it starts at the outer layers of the disk and makes its way to the galaxy center. The stripping slows down upon reaching the galactic bulge because the denser gas is better bound by gravity and the greater amount of gas naturally takes longer to get stripped. Some of the stripped gas can fall back into the galaxy, some of it continues its journey leaving the galaxy for good and forming a tail behind it.

The effect of RPS depends on multiple parameters. The pressure created depends on the density of the ICM and the velocity of the galaxy relative to the cluster. The bigger the density or velocity the bigger the force. More massive clusters have denser ICM. The density in a cluster is not uniform, the ICM gets denser closer to the cluster center. We specify the distribution of the ICM using a β-profile in section 5.3. Also, the velocity increases the closer the galaxy orbits the center. This means the force produced is strongly dependent on the trajectory of the galaxy.

Different galaxies react differently to the same pressure. More massive galaxies have stronger gravitational hold onto the diffuse gas and do not let it escape. Moreover, a galaxy can be oriented in many ways in respect to its movement. When the velocity vector points near the galactic equator we speak of edge-on stripping. On opposite side, face-on stripping happens when the velocity vector points near the galactic pole.

The disturbance inflicted onto the hydrogen component can induce a collapse of the molecular clouds in the disk leading to an increase in star formation, known as starburst. The stripped gas in the tail can also bunch up and create molecular clouds capable of star formation. The star forming tail is then visible in the optical band and bears resemblance to the tentacles of a jellyfish, the disk playing the role of the jellyfish head. Such galaxies got nicknamed jellyfish galaxies.

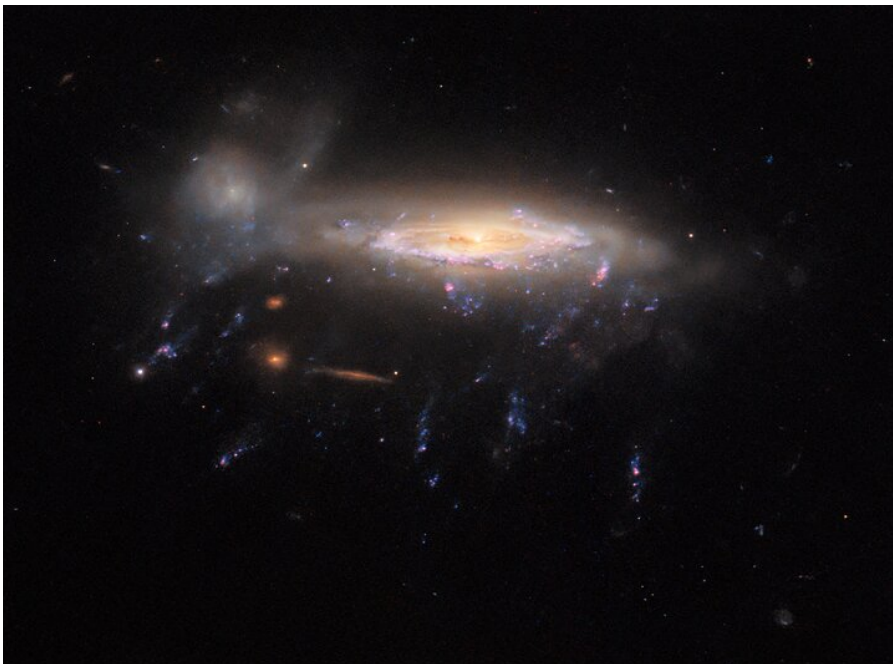

Figure 7: An optical image of the jellyfish galaxy JO204 in the constellation Sextans. Credit: ESA/Hubble & NASA, M. Gullieuszik and the GASP team

Section 3:

Observations

Written with the information from Yagi et al. (2010), Jáchym et al. (2017), Cortese, Catinella, and Smith (2021).

We aimed to observe the molecular component and study the effects of the RPS process in two galaxies in the Coma cluster, the galaxies D100 and GMP2374. The Coma cluster is a rich galaxy cluster with the total mass of $1–2 \times 10^{14}\,M_{\odot}$, more than 2000 galaxies, a high galaxy velocity dispersion of about $1100\,km\,s^{-1}$, which means the hydrodynamical influence of the intra-cluster medium is expected to have a strong impact. At nearly 100 Mpc, it is also the nearest rich galaxy cluster, providing good conditions for high-resolution observations. Previous observations, shown in Figure 9, uncovered signs of an RPS event taking place in both of the galaxies.

3.1 D100

This galaxy shows a clearly visible sign of an ongoing RPS event, with a strongly asymmetric dust component being stripped from the center, forming a brownish veil of extinction that covers a fraction of the galactic disk visible in Figure 9. Observing in the optical Hα filter allows us to map the warm ionized gas component. It revealed a long tail of stripped material and a galactic disk devoid of any emission, except of the nuclear disk region. It is worth noting that the tail is much narrower than the optical disk of the galaxy. This indicates the galaxy is in an advanced stage of the RPS process, where the galactic disk has been nearly completely stripped of the gas component, leaving mostly only the stellar component. The tail also shows only very little flaring, suggesting that the stripping radius has not changed much over a longer period of time. This supports the idea that the shrinkage of the stripping radius slows down at disk radii close to the galactic bulge.

With the strongly gas-truncated disk, the galaxy D100 is likely at the late stage of its transformation towards passive S0-type. Previous observations using the IRAM 30m millimeter single-dish telescope have revealed the RPS tail of D100 contains large amounts of molecular gas.

3.2 GMP2374 (NGC4911)

Looking at the images in Figure 9, we find the effects of an RPS event are much less obvious than in D100. The stellar disk is rather symmetric (besides the giant hole at the left side of the disk), with a lot of young star formation, and dust

extinction features (brown colour) that mostly follow the stellar disk. The Hα image reveals some stripping of warm ionized gas component, though not as drastic as in D100. The galactic disk still holds most of the gas component, but we also see some emission leaving the disk in the south-east direction. The GMP2374 galaxy is likely at a much earlier stage of RPS compared to D100.

3.3 Tracing H_2 gas with the CO(2-1) line

Our goal is to trace the molecular hydrogen component in the two galaxies and study the effects of RPS. Unfortunately, direct observations of molecular gas are difficult. The H_2 being a symmetric low-mass molecule with no dipole moment, it has trouble emitting radiation at the low temperature in molecular clouds typically below 50 K. Observations of Carbon Monoxide (CO) rotational lines are usually used as an indirect indicator of the occurrence of the H_2 gas. Carbon Monoxide is the next most abundant molecule after H_2.

In our observations we observed the CO(2-1) line, emitted due to the J = 2 –> 1 rotational transition at 230.5 GHz (1.3 mm). We have to account for the Doppler shift caused by the radial velocity of the objects relative to the Earth and match the spectral setup of our observations to the shifted line. For D100 with a radial velocity of 5306 km s^{-1} the line is shifted to about 226 GHz, the GMP2374 has a radial velocity 8004 km s^{-1} and the line lies at about 224 GHz.

Table 1: Basic parameters of the galaxies D100 and GMP2374

	D100	GMP2374
RA (J2000)	$13^h00^m09.14^s$	$13^h00^m56.06^s$
Dec (J2000)	$+27°51'59.34''$	$+27°47'27.15''$
Redshift	0.0177	0.0267
Radial velocity [km s^{-1}]	5306	8004
Stellar mass[1] [10^8 M$_\odot$]	21	1500
Projected distance from Coma center [kpc]	233	532
Optical diameter [kpc]	3.3	19.6
Inclination	45°	34.7°

[1]MEDIAN stellar mass in the MPA-JHU SDSS catalog (Yagi et al. 2010)

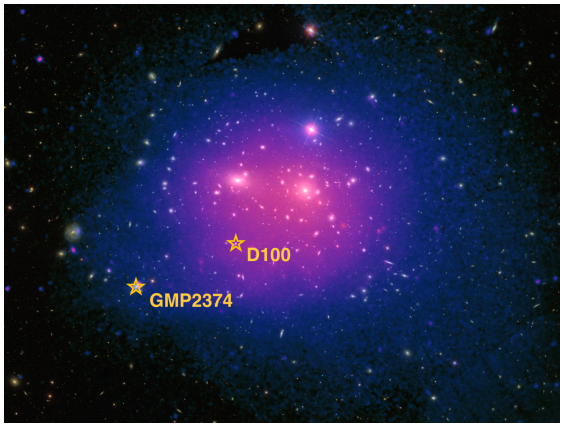

Figure 8: Location of the two galaxies in the central parts of the Coma galaxy cluster displayed in X-ray and optical light, as seen by XMM-Newton and the Sloan Digital Sky Survey (SDSS). Credit ESA/XMM-Newton/SDSS/Sanders et al. (2020).

Figure 9: Images of the observed galaxies taken by the Hubble Space Telescope (HST), top left: D100 on the right side of the image, top right: GMP2374 at the top of the image, bottom: Hα observations from the Subaru telescope (Yagi et al. 2010) overlaid over the Hubble images showing the distribution of warm ionized gas

Section 4:

Data Processing

Written with the information from Högbom (1974), Cortes et al. (2023), CASA Team and Associated Universities (2021).

We used ALMA telescope data from the project *ALMA JELLY - Survey of Nearby Jellyfish and Ram Pressure Stripped Galaxies* (PI[1] Jachym), which are accessible in the ALMA Science Archive at almascience.eso.org/aq under the project ID 2021.1.01616.L. The observations were set up in the following way: two spectral windows aiming at capturing line emission, one for the CO(2-1) line, the other for the CS(5-4) line, in the Frequency Division Mode (FDM) with a high frequency resolution and two spectral windows for measuring the continuum in the Time Division Mode (TDM). Table 2 summarizes the parameters of the spectral windows. In this work we focus only on the CO(2-1) observations. Both the main array of 12m antennas distributed in a compact configuration with minimum and maximum baselines of 15 m and 500 m, respectively, and the ACA 7m compact array were used for the observations.

The wide band width of 2 GHz allowed us to securely cover the radial velocity of all components of the galaxy – the stripped gas is slowed down relative to the galaxy cluster by the ICM and its emission is shifted in frequency accordingly.

Notable is the difference in the number of channels and their velocity width between line and continuum measurements. The line spectral windows (in the FDM mode) contain more channels to provide a better resolution in frequency and velocity. Channel velocity width of $1.292\,\mathrm{km\,s^{-1}}$ means we could differentiate two parts of the galaxy, whose velocities differ only by that amount.

4.1 Calibration pipeline

The interferometric method needs very precise measurement and every little variation in the observing conditions can significantly affect the result. Some conditions change in the timeframe of a single measurement block and the resulting data needs to be calibrated to produce a correct image.

This process can be simplified as the changes are not tied to each baseline, but to individual antennas. Storing information about each antenna and not each baseline significantly reduces the amount of data needed for calibration. Phase calibration can be further simplified by choosing one of the antenna to be a reference antenna, whose phase is defined to be always zero in all spectral channels.

[1]PI = Principal Investigator

Table 2: Parameters of the spectral windows used in our observations.

D100						
Transition	Center frequency	Bandwidth		# of channels		Channel vel. width
		12m	7m	12m	7m	
CO(2-1)	226.512 GHz	1.875	2 GHz	1920	2048	$1.292\,\mathrm{km\,s^{-1}}$
cont.	228.253 GHz	2	2 GHz	128	128	$20.522\,\mathrm{km\,s^{-1}}$
CS(5-4)	240.648 GHz	1.875	2 GHz	1920	2048	$1.217\,\mathrm{km\,s^{-1}}$
cont.	242.392 GHz	2	2 GHz	128	128	$19.325\,\mathrm{km\,s^{-1}}$

GMP2374						
Transition	Center frequency	Bandwidth		# of channels		Channel vel. width
		12m	7m	12m	7m	
CO(2-1)	224.556 GHz	1.875	2 GHz	1920	2048	$1.304\,\mathrm{km\,s^{-1}}$
cont.	226.264 GHz	2	2 GHz	128	128	$20.703\,\mathrm{km\,s^{-1}}$
CS(5-4)	238.577 GHz	1.875	2 GHz	1920	2048	$1.227\,\mathrm{km\,s^{-1}}$
cont.	240.306 GHz	2	2 GHz	128	128	$19.493\,\mathrm{km\,s^{-1}}$

There are many influences that cannot be predicted and require calibration measurements. One of these is water vapour in the atmosphere, that can affect each antenna differently and can change drastically in a short time. It can introduce an unexpected phase shift or absorb some of the radiation causing an error in amplitude. Each antenna is equipped with a Water Vapour Radiometer that measures the water vapour every 1.1 seconds to correct the phase fluctuations.

An important step is the system temperature (T_{sys}) measurement, that checks the antenna sensitivity and the background radiation of the sky. It consists of a short 15-second procedure, that places a hot plate (80 °C) or a plate of ambient temperature in front of the receiver or lets a free view of the sky and measures the response.

During observations some of the observing time is reserved for measuring calibration sources. These are stable point sources with very accurate position measurements, known flux densities and spectra. The antenna switches between the science target and the calibration source several times over the measurement to correct for the effects caused by the unstable atmosphere.

Nowadays, over 95% of data acquired by ALMA is processed by the automatic pipeline (the remaining fraction of the data are processed manually). Pipeline processing that is done through the SW package Common Astronomy Software Application (CASA, McMullin et al. 2007) includes calibration and imaging of the data. All data that achieve the project-requested sensitivity and angular resolution are delivered to the authors of the observing projects (PI). The pipeline checks

for faulty data or antennas, removing them from the dataset, and calibrates the data using calibration measurements to correct for effects of the instrument itself (mainly bandpass and system noise), effects of the atmosphere (gain calibration), and to scale to the correct flux.

In the imaging part, the pipeline is reconstructing the image from the calibrated visibilities. It first identifies channels where no source line emission was found and makes a continuum model. This continuum is then subtracted from the calibrated datacube. Lastly the pipeline is able to produce images from the data by using deconvolution by CLEAN method. We skipped this last step because we aimed to perform the imaging of the interferometric data manually. This was one of the main goals of this work. Re-imaging of the pipeline-calibrated data is often necessary since the delivered images are not of suitable quality or parameter setting for intended science analysis.

The pipeline process is summarized in a Weblog that is available in the ALMA Science Archive together with the data. It describes individual steps and displays warnings if something is out of the ordinary (like a high fraction of flagged antennas). An example graph from the weblog is shown in Figure 10. We used the weblog to survey the calibration steps, as well as to check whether the continuum channels were determined correctly and no line emission was present in the continuum model.

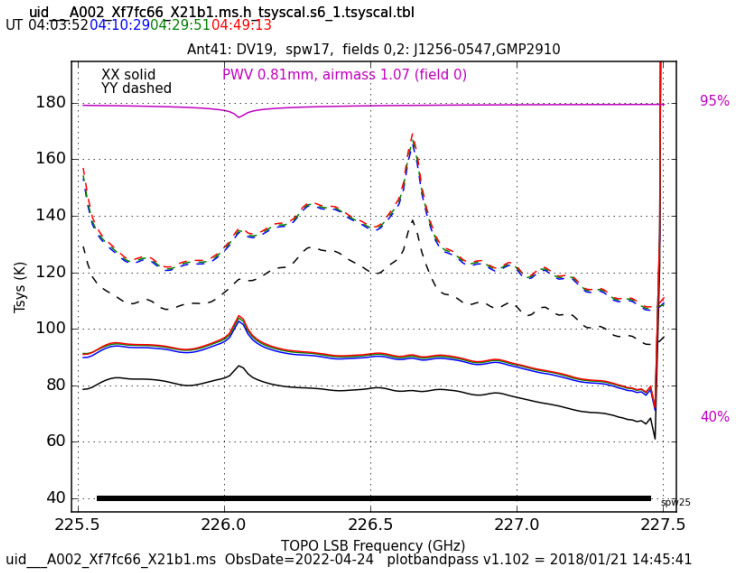

Figure 10: An example of the amplitude calibration measurement of a flagged antenna. The system temperature in the yy polarization (dashed lines) is about 40 K above the rest of the antennas.

4.2 Cleaning

The resulting image is cut into the velocity channels. That means it has three axes – two regular x, y axes and a third, velocity axis. Because of this we call it an image cube.

Only the CO(2-1) line spectral window contained source emission, the CS(5-4) line remained undetected. We extracted it from the whole dataset to reduce the size and simplify work. The dataset was also divided into two sets, one measured by the 12m antennas and the other by the 7m antennas. We created three subsets for further cleaning. One for D100 with combined data from both 12m and 7m antennas, one for GMP2374 with combined data and one for GMP2374 with only the 7m data, to better capture diffuse emission.

An interferometer measures a quantity known as the complex visibility, which is the Fourier transform of the intensity distribution on the sky. Thus, the sky brightness distribution is the inverse Fourier transform of the complex visibility distribution in the visibility plane. Since the visibility plane is not fully sampled, in principle an infinite number of images are consistent with the data.

The first step is to make a "dirty image", i.e., a convolution of the sky brightness distribution with the dirty beam, where no actual cleaning is done. It allows us to take a detailed look at the channels and again pick only those where emission is found to reduce the runtime of the process. We can also determine the signal strength and RMS noise of the image, which are crucial parameters for the cleaning process. The dirty image will be improved by deconvolution techniques which minimize the effect of the incomplete spatial sampling, such as the CLEAN algorithm.

With the narrowed set of channels and correct parameters we proceed to an iterative cleaning process. It is done through the CASA command *tclean*. The process consists of two cycles, the major and the minor cycle, their relation is shown in Figure 11. The major cycle first transforms the complex visibility into the sky brightness distribution and inputs it into the minor cycle. Here the image is deconvolved to make a model of the emission, which is convolved with the dirty beam and subtracted from the residual image. When the peak residual reaches the first sidelobe level the minor cycle stops and gives the model image back to the major cycle. The model image is transformed back into the complex visibility domain and subtracted from the data to produce the residual, which is used in the next run of the cycle. The major cycle stops when the peak residual reaches a specified threshold.

Our role in this process is to differentiate between actual emission and artificial features such as high noise or sidelobes. We could mark these regions manually, but given the number of channels and iterations it was sensible to use tools that automate this process. We used the *auto-multithresh* masking method implemented directly in CASA. It looks for regions by comparing the signal to the RMS noise

of the image. When it exceeds a given threshold it adds the region into the clean mask and treats it as real emission.

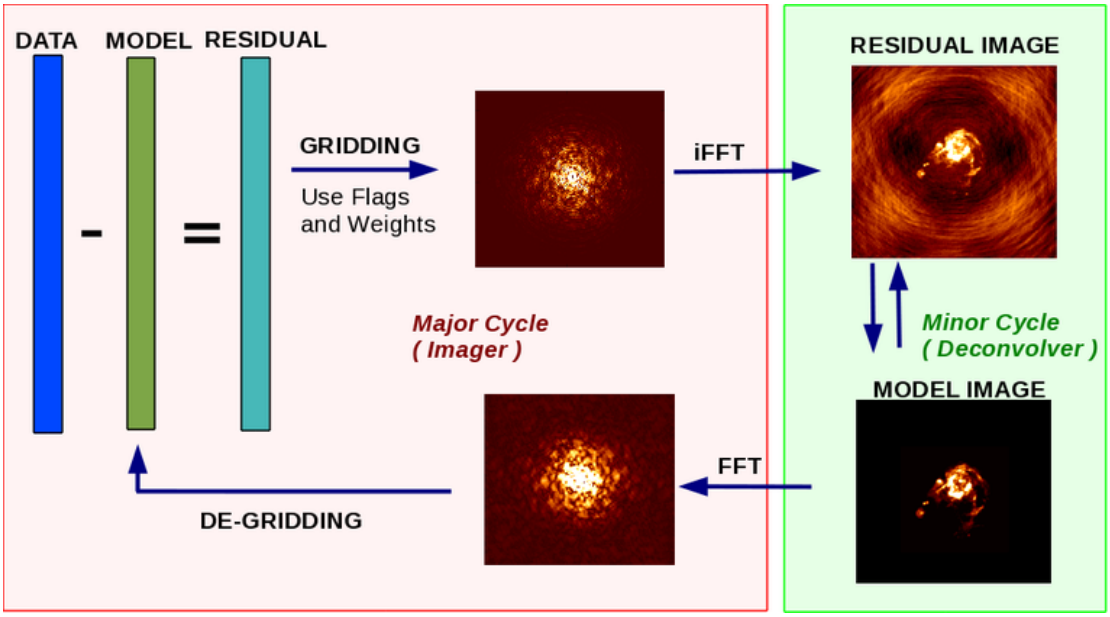

Figure 11: The cleaning process: the major and minor cycle of the tclean command Taken from: https://casadocs.readthedocs.io/en/stable/api/tt/casatasks.imaging.tclean.html#description

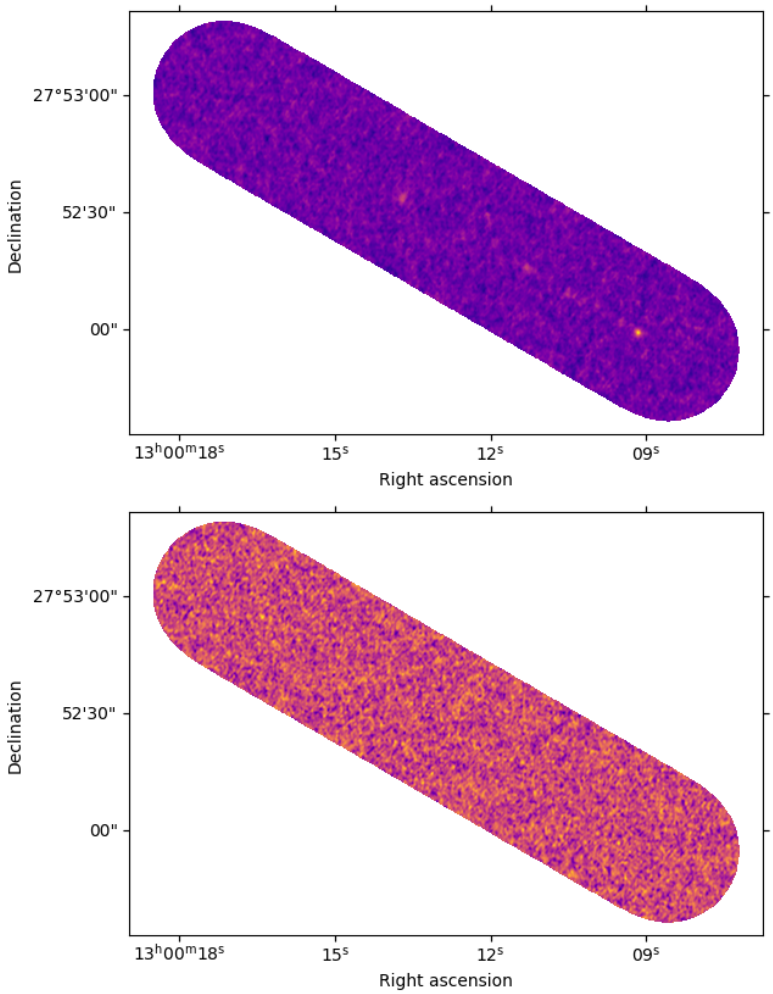

Figure 12: Top: an example of one channel of the "dirty image" of the galaxy D100, bottom: residual image produced during the cleaning process of the galaxy D100 showing no leftover line emission

Here is an example of the most important parameters used in the *tclean* command used for cleaning in CASA.

```
Data parameters
vis                 = 'combined.ms/'
spw                 = ''
imagename           = 'GMP2374_line'
Image parameters
imsize              = [800, 800]
cell                = 0.17
phasecenter         = 14
Spectral parameters
specmode            = 'cube'
nchan               = 90
start               = '7550km/s'
width               = '5km/s'
restfreq            = '230.536GHz'
Deconvolution parameters
gridder             = 'mosaic'
weighting           = 'briggs'
robust              = 0.5
threshold           = '4mJy'
Masking parameters
usemask             = 'auto-multithresh'
sidelobethreshold   = 2
noisethreshold      = 4.25
lownoisethreshold   = 1.5
negativethreshold   = 0.0
minbeamfrac         = 0.3
```

The term *vis* refers to the visibility file. The line *spw* determines which spectral windows to use in the cleaning, since we already extracted the right ones earlier we left it empty to use all present in the datafile. *Imagename* sets the name of the resulting image and all of the products of the cleaning process, such as the residual, the PSF etc.

Imsize is the size of the image in pixels. The size of a pixel in arcseconds must be input in the *cell* parameter. The correct value can be calculated by a simple equation: $206265/b_{\max}/n$, where $b_{\max}$ is the longest baseline in wavelengths and n the number pixels across the beam (usually 5-8 pixels). *Phasecenter* is the id of the pointing in the phase center of the image, usually placed into the middle of the mosaic.

Specmode sets the spectral definition mode, `'mfs'` is used for continuum imaging with only one output spectral channel, we used `'cube'` to obtain a imagecube with multiple channels. We have to specify the spectral settings of the cleaning. *Start* marks the first spectral channel to include in the imaging (can be input either as the channel number or its frequency or its velocity) and then includes *nchan* following *width*-wide channels. The *restfreq* is the rest frequency of the line.

The *gridder* parameter sets the projection method used for gridding the measured visibilities onto a regular uv-grid. We can define the weighting of the visibilities in the uv-plane with the *weighting* parameter, which can have a strong impact on the resulting image. `'Natural'` weighting takes data weights from the dataset, offers high sensitivity but can generate a wide PSF with high sidelobes. `'Uniform'` weighting treats all datapoints equally, produces a narrow PSF with weak sidelobes but offers lower sensitivity. We used the `'briggs'` method that combines the two algorithms according to the *robust* parameter, where $robust = 2$ corresponds to `'uniform'` and $robust = -2$ results in the `'natural'` weighting. We set $robust = 0.5$ which is a good trade-off between resolution and sensitivity. The deconvolution process stops when the peak value in the residual image falls under the value set by *threshold*.

The masking method used in the cleaning process was set to `'auto-multithresh'`. The automatic algorithm uses multiple thresholds. The sidelobe level is multiplied by the *sidelobethreshold* and compared to the signal-to-noise level multiplied by the *noisethreshold*. Whichever is higher is used for creating the initial mask. We can filter out spikes of noise reaching above the threshold by removing any regions smaller than a fraction of the beam size, set by the *minbeamfrac* parameter. The initial mask is then expanded into regions that rise above the signal-to-noise level multiplied by the *lownoisethreshold*. *Negativethreshold* is used for imaging absorption features. We did not expect any, so we left this parameter at 0.

With the above setup of tclean, we were able to produce a clean datacube with the synthesized beam of 1.33 arcsec $\times$ 0.83 arcsec (i.e., 0.6 kpc $\times$ 0.4 kpc) and an RMS sensitivity of 1.7 mJy / beam.

4.3 Moment maps

In order to analyze the spectral line in the resulting three-dimensional clean datacube, one may "collapse" the velocity axis, i.e., generate moments of the spectral axis.

$$M_0 = \Delta\nu \sum I_i \tag{4}$$

$$M_1 = \frac{\sum I_i \nu_i}{M_0} \tag{5}$$

$$M_2 = \sqrt{\frac{\sum I_i (\nu_i - M_1)^2}{M_0}} \tag{6}$$

When creating the moment maps, we prefer not to include the whole image and the full range of channels. Instead, we identify only source emission and exclude any surrounding noise as it corrupts the result. For this we used the *maskmoment*[2] python package. Similar to the cleaning algorithm, it detects real emission by comparing it to the RMS noise of the image and checking whether it rises above a given threshold.

In the 0th moment (the integrated intensity) map, we are integrating pixels through each of the velocity channels. Shown in Figure 13 are the integrated moment maps. They provide a view of the distribution of the CO emission tracing the molecular gas in the galaxies.

We see the molecular gas in the tail of D100 is clearly detected and follows the distribution of the warm ionized gas as traced by the Hα measurements in Figure 9, but forms clumps. The most distant detected clump at the very end of the tail is at about 60 kpc from the galaxy. The individual clumps are mostly not connected by areas of lower density as is the case in the Hα emission. This might be an intrinsic property of the CO emission distribution in the tail, or due to insufficient sensitivity of the image. Imaging with more natural weighting, or future deeper observations could reveal the more diffuse component. The detailed look at the disk of D100 reveals a strongly truncated and asymmetric disk and the stripped gas escaping into the innermost parts of the tail. The connection between the disk and the inner tail is formed by a narrower 'bridge' at the northern edge of the structure, and is consistent with the morphology of the dust extinction feature visible in Figure 9. The radius of the truncated CO disk is similar to that of the Hα emission.

The combined data of GMP2374 shows a high-resolution image of the galactic disk. In the leading edge of the disk we see a strongly stripped region (a "hole") between the galactic arms. We can also see material getting stripped at the opposite edge, in the form of unwinding spiral arms, and a clump of gas beneath the galaxy,

[2]https://github.com/tonywong94/maskmoment

which might be a leftover of a more extended spiral arm originally located at the bottom-left (south-west) side of the disk. The 7m data uncover the weak emission of more diffuse gas forming a short tail behind the galaxy.

We also produced 1st moment (the intensity weighted coordinate) maps. They show the velocity distribution of the emission. We made velocity maps of galaxy disks of both galaxies and of the stripped matter in the tail of D100. The produced velocity maps are shown in Figure 14. In the top image we see how the stripped gas is slowed down in the ICM, with a velocity difference of about $200\,\mathrm{km\,s^{-1}}$ over the length of the tail of about 60 kpc. The detail of the D100 disk shows a remnant of the galactic rotation in the recently stripped gas and a clear imprint of the galaxy rotation in the inner tail. The 7m data velocity map of GMP2374 shows us from which part of the galaxy has the gas been stripped.

The velocity dispersion of the galaxies is represented by the 2nd moment (intensity weighted dispersion of the coordinate) maps. They highlight areas with a wide range of velocities. Looking at the Figure 15, we can see that in most clumps in the tail of D100 the velocity dispersion does not differ much and is of the order of 10–$20\,\mathrm{km\,s^{-1}}$. However, one spot in the tail exhibits high velocity dispersion. This might correspond to overlapping clumps with different velocities, or to a point in the tail where the hydrodynamic character of the interaction causes a local increase in turbulence. It is easy to recognise the galactic centers in the images, because the range of velocities is wider than in the galactic disk. In the bottom right image, the high velocity dispersion at the bottom edge of the disk signals that two regions of differing velocities overlap there.

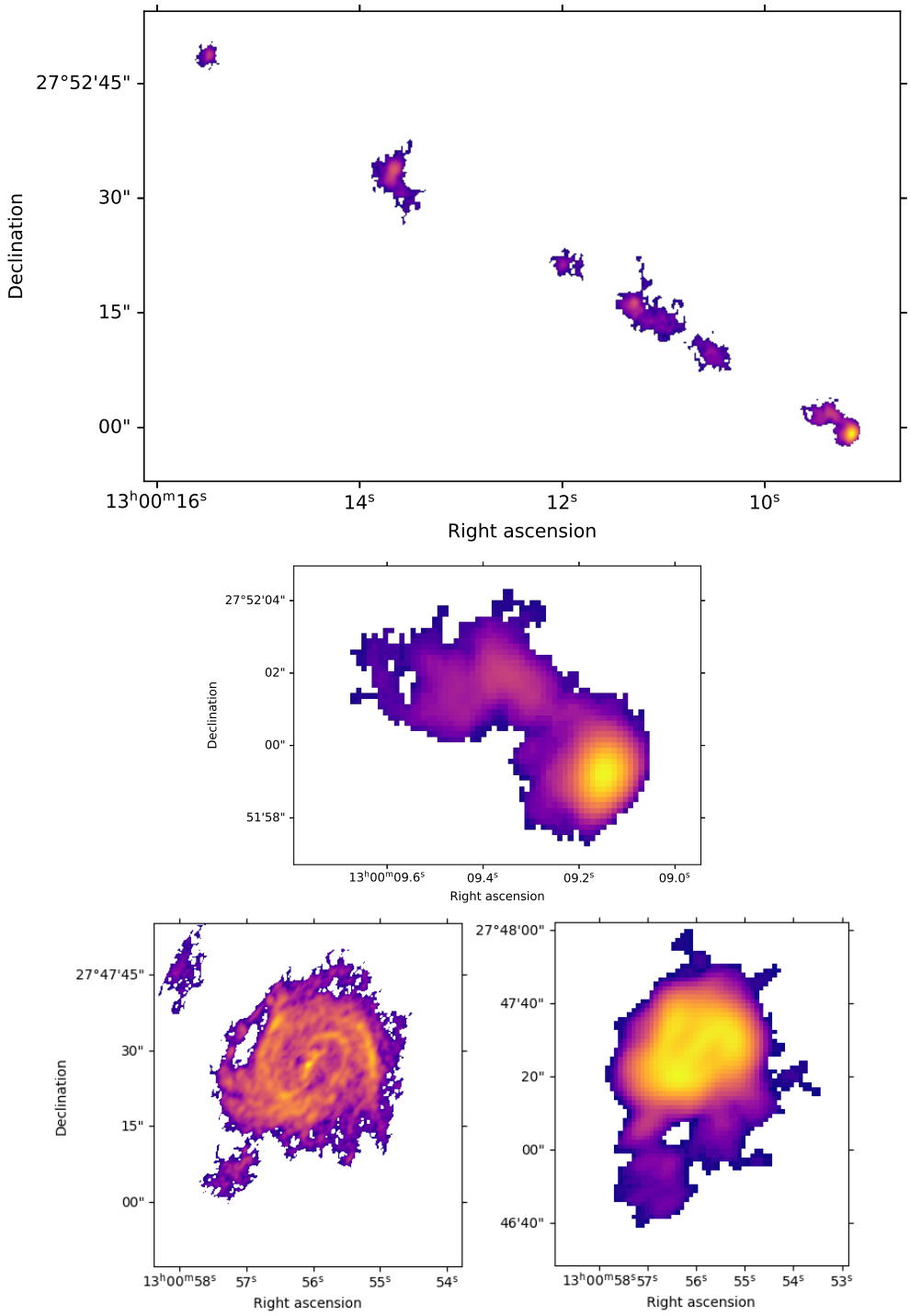

Figure 13: 0th moment maps, top: the galaxy D100 and its tail, combined data; middle: detail of the galactic disk of D100, combined data; bottom left: GMP2374 combined data (emission in the top left is a noise artifact); bottom right: GMP2374 7m data

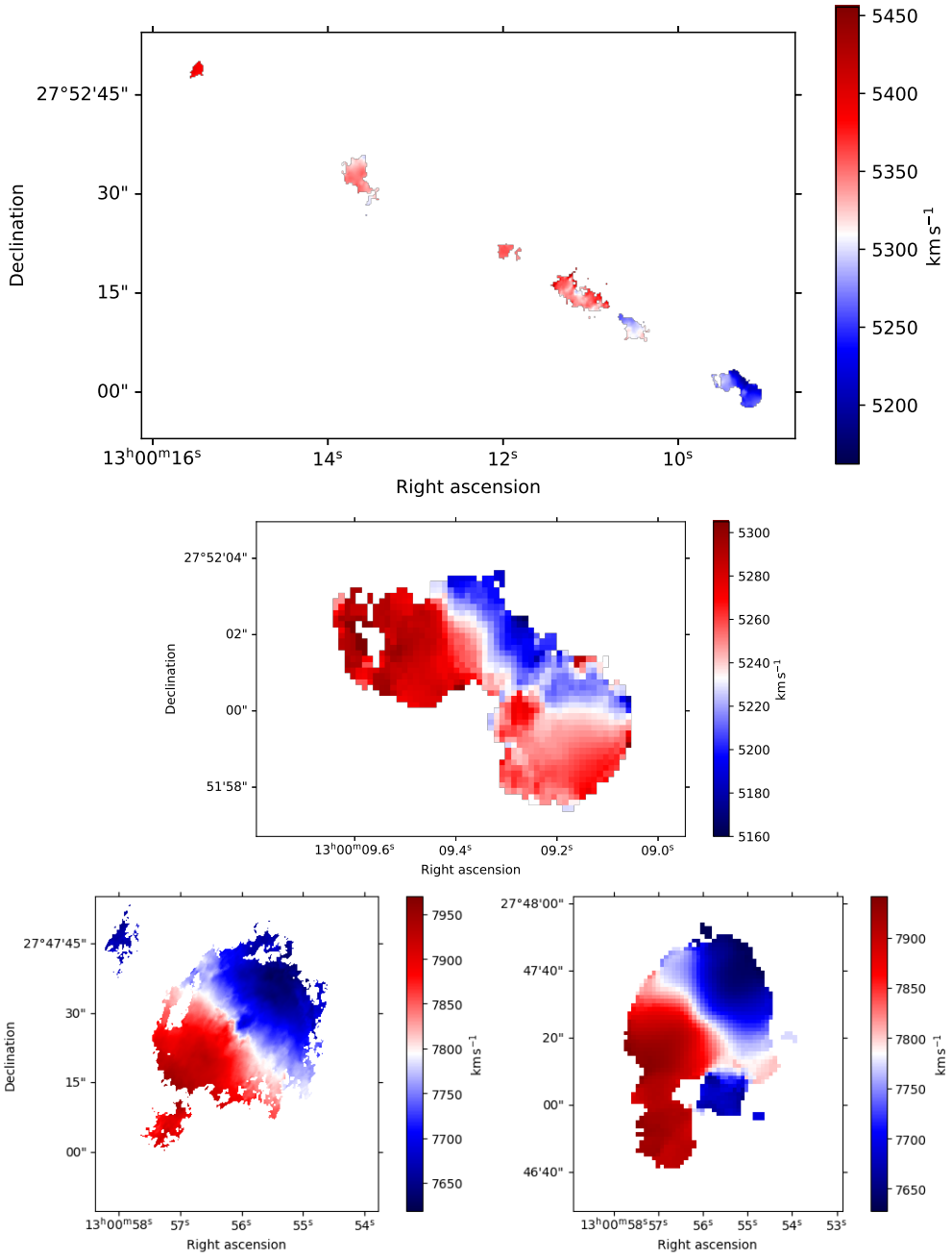

Figure 14: 1st moment maps, top: the galaxy D100 and its tail, combined data; middle: detail of the galactic disk of D100, combined data; bottom left: GMP2374 combined data (emission in the top left is a noise artifact); bottom right: GMP2374 7m data

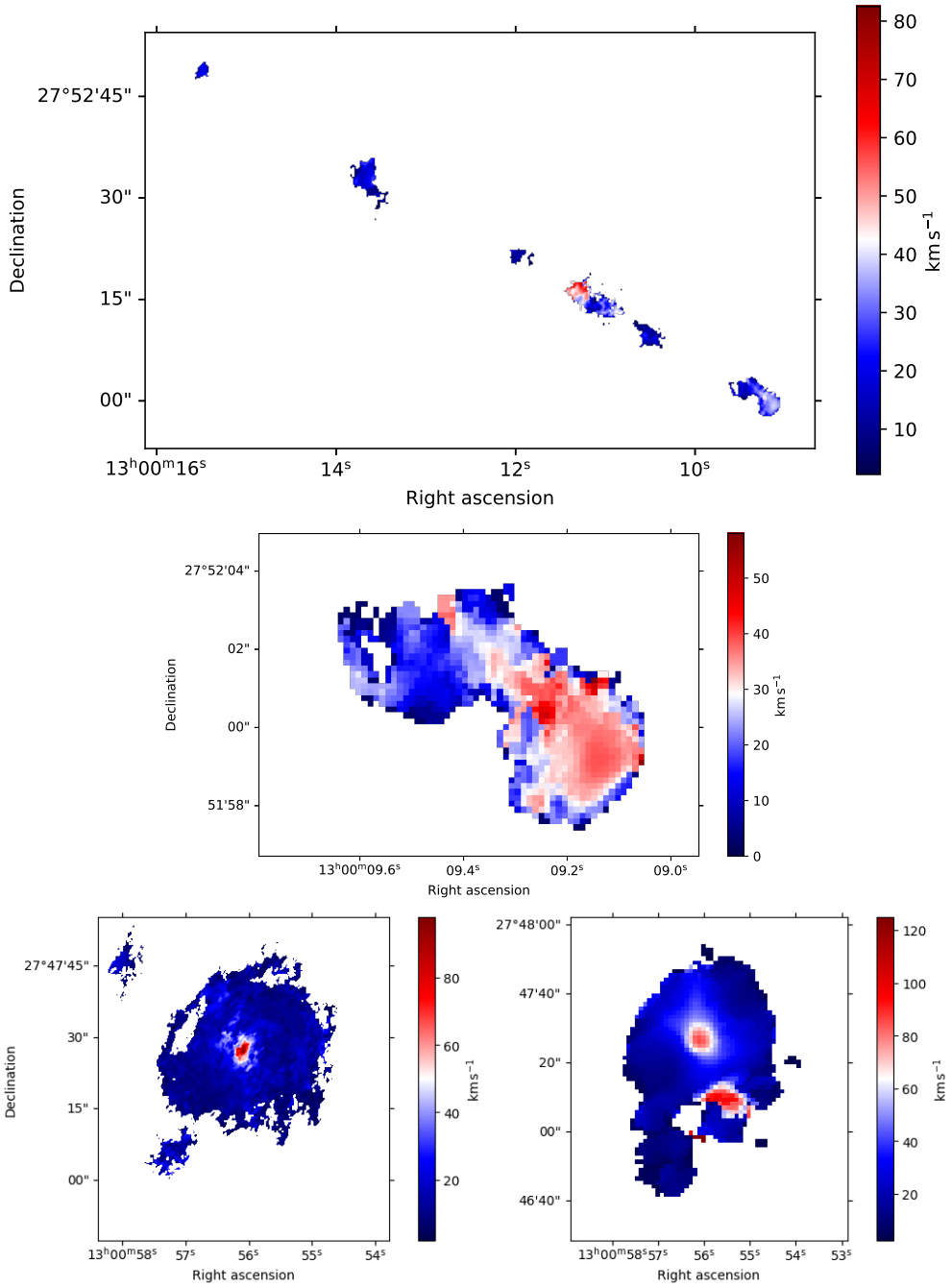

Figure 15: 2nd moment maps, top: the galaxy D100 and its tail, combined data; middle: detail of the galactic disk of D100, combined data; bottom left: GMP2374 combined data (emission in the top left is a noise artifact); bottom right: GMP2374 7m data

4.4 PV diagrams

An interesting way to further analyze the data is through position-velocity diagrams. One defines a line in the x-y (RA-Dec) plane and makes a slice of the image cube along that line in the velocity axis. On the x-axis of the diagram the position along the line is plotted and on the y-axis the corresponding velocity channels, the pixel values then depict the signal strength. One can make an average of pixels perpendicular to the line, the number of pixels averaged is given by the width parameter. For D100 we set width = 3 pixels, for GMP2374 width = 10. The PV diagrams were made in Carta, along the major and minor axes of both galaxies and for the tail of D100, shown in figs 16, 17. In the case of the galaxy axes, the lines are centered on the galaxy center, meaning OFFSET = 0 equals galaxy center.

For the major axis of D100 there is a very weak trend in the radial velocity due to the galactic rotation, but due to the strongly truncated gas disk, the PV diagram is significantly dissimilar to typical rotating disks. The PV diagram of the minor axis indicates a slight offset of the molecular component from the center of the galaxy. The interesting part is the tail (Figure 17), where we see the distribution of velocity of the various clumps. It mostly follows a linear trend, meaning that the farther it is from the center the more it is slowed by the ICM. However, we also see some exceptions around the offset of around 5 and 15 arcsec, that have higher radial velocity compared to the neighbouring clumps. The two clumps at the 15 arcsec offset explain the high velocity dispersion seen in the Figure 15.

The PV diagrams of the GMP2374 have a typical shape for galactic disks. Along the major axis we see a roughly S-shaped profile corresponding to the two sides of the disk that have different radial velocities due to the rotation of the disk. The outer wings of the profile are disturbed and asymmetric due to the RPS interaction. In the minor axis we recognise some asymmetry, where the emission at the leading edge looks a bit squished, while the following edge is stretched out. There also is a clump of slower matter in the galactic center.

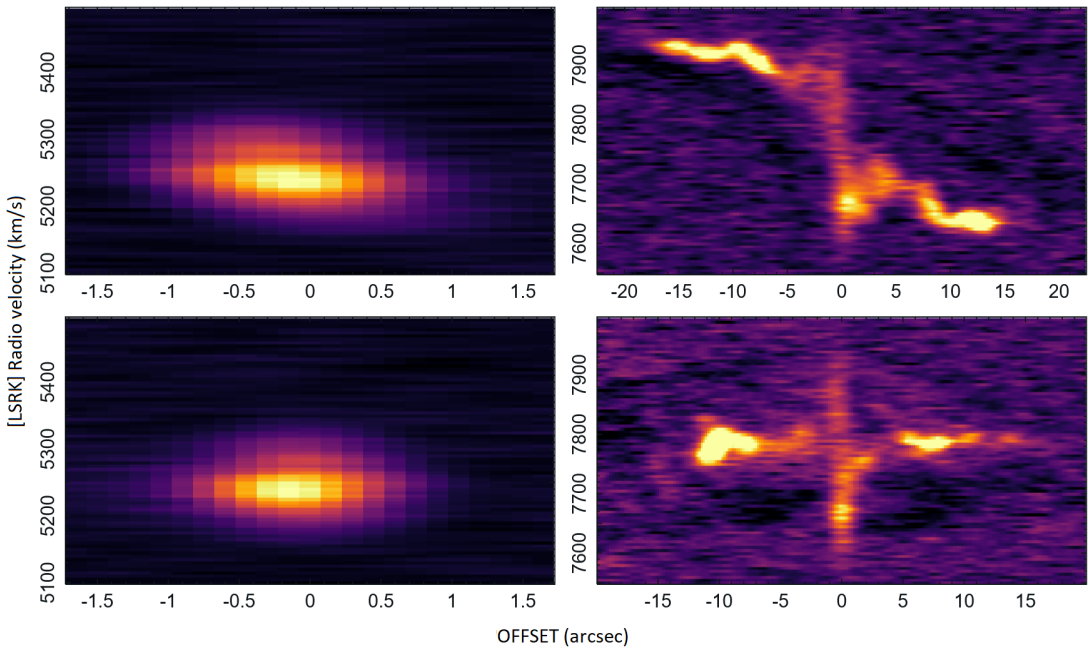

Figure 16: P-V diagrams, top left: major axis of D100, offset axis points north image-wise, bottom left: minor axis of D100, offset axis points east, top right: major axis of GMP2374, offset axis points north-east, bottom right: minor axis of GMP2374, offset axis points south-east

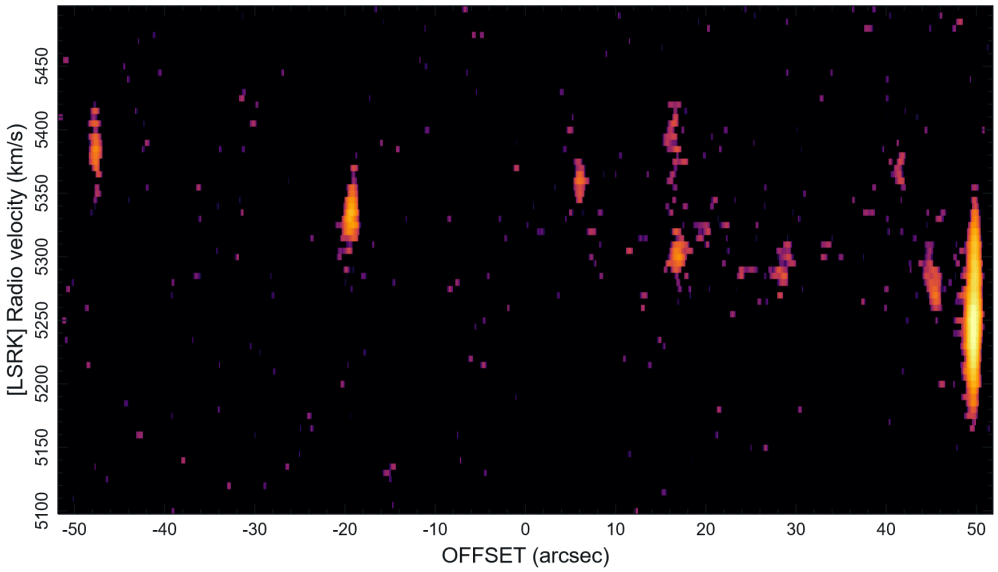

Figure 17: P-V diagram of the stripped tail of D100, galaxy disk on the right of the figure

Section 5:

Results

In this section, we will further analyze the molecular gas content of the two galaxies and suggest what are the main reasons for the observed differences. The intensity maps presented in the previous section clearly indicated that the galaxies are in very different evolutionary states of the ram pressure stripping interaction and also in different states of their evolution. GMP2374 shows an extended molecular disk with only mild asymmetric features, and rather normal velocity field and PV diagrams. D100, on the contrary, has a very disturbed morphology with strongly restricted distribution of the molecular gas in the disk, a long one-sided molecular tail, and strongly perturbed PV diagrams.

There are several parameters that determine the effects of the interaction: those of the galaxies, especially the galaxy mass that determines the gravitational restoring force that anchors the interstellar matter in the galaxies, and those of the cluster, especially the distribution of the ICM and orbital velocities of galaxies (velocity dispersion) that determine the strength of the ram pressure. Since both our galaxies are in the same cluster, the main difference is given by their orbits in the cluster and thus their current clustercentric radius and orbital velocity. In the following table we summarize the important parameters, as well as measures of the ram pressure interaction. Especially, the stripping radius which is the radius of the gas disk at the side facing the ICM wind, and the tail length which we define as the difference of the distance of the tip of the tail and the stripping radius. The estimates of the current and the maximum ram pressure are calculated in a following subsection.

There is an important difference in the mass of the two galaxies, with GMP2374 being almost two orders of magnitude more massive. The interstellar matter strengthens the gravitational bonds, rendering the ram pressure ineffective.

Moreover, GMP2374 is projected to more than two-times larger distance from the cluster center, where the ICM density is three–times smaller. The radial velocity of D100 relative to the cluster mean is larger (cca 1600 km/s) than that of GMP2374 (cca 1100 km/s). It is interesting that both galaxies have the tails oriented so that the angle between the tail and the direction to the cluster center is close to perpendicular. In the case of D100 it has been suggested that it is near its pericenter (Jáchym et al. 2017).

All this indicates that D100 is in a much more advanced state of ram pressure stripping of its gas content.

Table 3: Physical properties of the galaxies D100 and GMP2374 and the ICM[1]

	D100	GMP2374
Radial velocity in Coma cluster [$\mathrm{km\,s^{-1}}$]	-1689	1009
Rotation velocity [$\mathrm{km\,s^{-1}}$]	131	246
Projected distance from Coma center [kpc]	233	532
Local ICM density [$10^{-27}\mathrm{g\,cm^{-3}}$]	3.4	1.1
Local ram pressure [10^{-11} $\mathrm{dyne\,cm^{-2}}$]	29	3.4
Maximum ram pressure [10^{-11} $\mathrm{dyne\,cm^{-2}}$]	69	3.5
Stripping radius [kpc]	0.6	7.1
Tail length [kpc]	59	21
Stellar mass [$10^8\,\mathrm{M_\odot}$]	21	1500
Molecular mass in disk [$10^8\,\mathrm{M_\odot}$]	1.9	117
Molecular mass in tail [$10^8\,\mathrm{M_\odot}$]	4.4	1.1

[1]Notes: Local ICM density = the ICM density at the projected distance of the galaxy from the cluster center, assuming an ICM beta profile (see 5.3); Local ICM pressure = ram pressure that corresponds to the local ICM density and the observed radial component of the galaxy's orbital velocity (corrected for its 3D shape); Maximum ram pressure = ram pressure that would be needed for stripping of gas at the observed stripping radius of the galaxy, assuming ram pressure matched the centrifugal force acting at a column density element; Tail length = most distant emission in Hα measurements (Yagi et al. 2010) Stellar mass = MEDIAN stellar mass in the MPA-JHU SDSS catalog (Yagi et al. 2010); Molecular mass in disk/tail = mass of the molecular component calculated from the CO line flux density (see 5.2).

5.1 Multi-phase gas stripping

It is important to study the molecular gas component in the context of other galaxy properties and the observations that are available from other wavelengths. Figure 18 shows for D100 and GMP2374 the Composite DECalS optical image using g-, r- and z-band data, the narrow-band Hα data (Yagi et al. 2010), together with our ALMA CO observations. It is interesting that in D100 the extent of the molecular tail is the same as the extent of the Hα tail. In GMP2374, the molecular gas is mostly in the disk, while the Hα tails is longer. This might be consistent with the difference in their evolutionary states: In GMP2374, the ram pressure is not efficient enough to strongly push denser components of the gas, in contrast with D100 where the interaction has been very efficient. The optical images also reveal that the two galaxies are of different types: while GMP2374 is clearly a late-type galaxy with active star formation in the disk, D100 is on its way towards passive, lenticular type. This is a direct consequence of the longer and stronger operation of ram pressure stripping of the D100 galaxy.

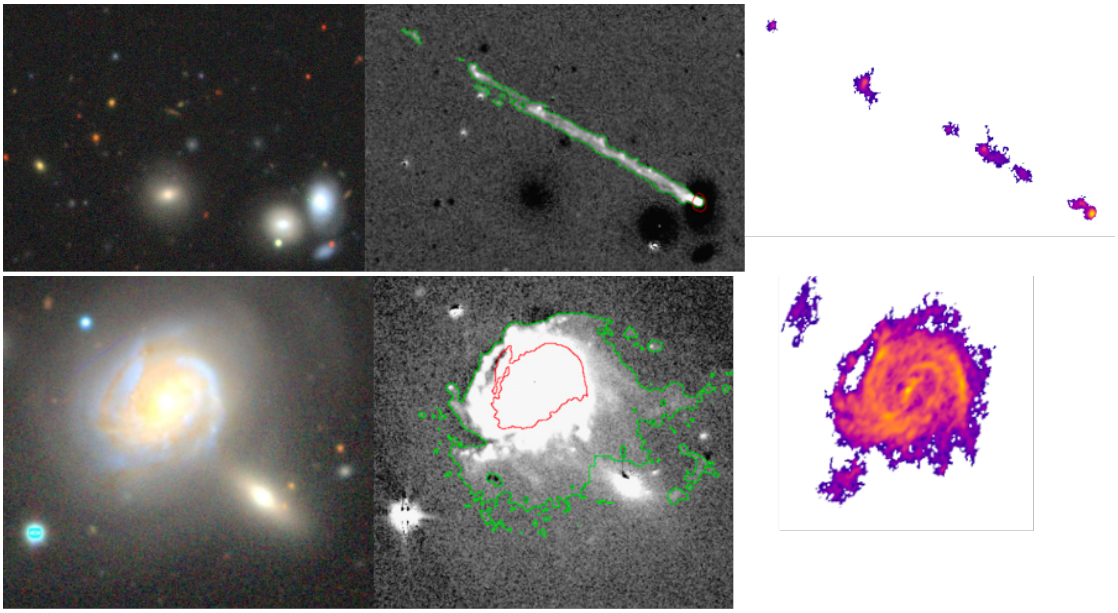

Figure 18: Images of the galaxies from comparison, left: the Composite DECalS optical image using g-, r- and z-band data; middle: Hα measurements from Yagi et al. (2010); right: our ALMA CO observations

5.2 Molecular mass in the galaxies and tails

Following Jáchym et al. (2017) we calculate the mass of the molecular gas corresponding to our CO observations. We want to measure the mass separately in the galaxy disk and in the tail. We therefore first measure the CO integrated flux within the radius corresponding to the stripping radius. Then, we measure the integrated flux outside of the stripping radius. The values of the stripping radii are given in Table 5.

From the standard relation of Solomon and Vanden Bout (2005), we calculate the CO luminosity following:

$$L'_{\mathrm{CO}} = 3.25 \times 10^7 \frac{S_{\mathrm{CO}}\,\Delta v\,D_{\mathrm{L}}^2}{\nu_{\mathrm{obs}}^2\,(1+z)^3}, \tag{7}$$

where L'_{CO} is the CO line luminosity in $\mathrm{K\,km\,s^{-1}\,pc^2}$, $S_{\mathrm{CO}}\,\Delta v$ is the CO velocity integrated line flux in $\mathrm{Jy\,km\,s^{-1}}$, ν_{obs} is the observed CO line frequency in GHz, and D_{L} is the distance in Mpc.

We calculate the corresponding molecular gas mass following

$$M_{\mathrm{H_2}}\,[M_\odot] = 5.5\,L'_{\mathrm{CO}}\,[\mathrm{K\,km\,s^{-1}\,pc^2}], \tag{8}$$

where we assume a CO-to-H_2 conversion factor of $2 \times 10^{20}\,\mathrm{cm^{-2}(K\,km\,s^{-1})^{-1}}$ that is standard under Milky Way disk conditions, the typical values for the CO(2–1)-to-CO(1–0) ratio of 0.8, and include a factor of 1.36 to account for helium.

We determined the velocity integrated line flux inside and outside the stripping radius from our Primary-beam-corrected images. We calculated the distances using the cosmological distance modulus from the HYPERLEDA database (Makarov et al. 2014). The calculated CO luminosities and molecular gas masses are shown in Table 4. The results are consistent with our previous observations. We see that the

Table 4: Calculated CO luminosities and molecular gas mass in the disk or the tail of the galaxies

		$L'_{\mathrm{CO}}\,[10^7\,\mathrm{K\,km\,s^{-1}\,pc^2}]$	$M_{\mathrm{H_2}}\,[10^8\,\mathrm{M_\odot}]$
D100	Disk	3.5	1.9
	Tail	8	4.37
GMP2374	Disk	210	177
	Tail	2	1.1

mass in the tail of D100 is more than two times higher than in the heavily stripped disk. On the other hand, the majority of the molecular gas of the GMP2374 is inside the stripping radius and only a fraction of the mass has been stripped into the tail. Also, the total mass of the molecular gas in the D100 is about 20 times lower than in the GMP2374, which was expected since the stellar mass of the GMP2374 is around two orders of magnitude higher. We can compare the total mass of the molecular gas to the stellar mass. The molecular mass in the D100 (around $7 \times 10^8\,\mathrm{M_\odot}$) makes up about half of the stellar mass ($21 \times 10^8\,\mathrm{M_\odot}$), but the molecular mass in the GMP2374 (around $180 \times 10^8\,\mathrm{M_\odot}$) accounts only for an eighth of the stellar mass ($1500 \times 10^8\,\mathrm{M_\odot}$). This difference could be explained by the formation of molecular hydrogen in the tail due to the disturbance of the atomic hydrogen by the ram pressure, which would result in an elevated mass ratio of molecular gas component to the stellar component.

5.3 ICM pressure estimate

The ICM pressure depends on its density and the speed at which the galaxy is moving through the ICM.

$$p_{\mathrm{ICM}} = \rho_{\mathrm{ICM}}\, v^2 \tag{9}$$

We approximated the ICM density distribution with a spherically symmetric, centrally-peaked β-profile (Cavaliere and Fusco-Femiano 1978):

$$\rho(r) = \rho_0 \left[1 + \left(\frac{r}{r_{\mathrm{c}}}\right)^2\right]^{-\frac{3}{2}\beta}, \tag{10}$$

where r is the distance from the cluster center, the central density $\rho_0 = 6.3 \times 10^{-27}\,\mathrm{g\,cm^{-3}}$, scale-length $r_{\mathrm{c}} = 260\,\mathrm{kpc}$ and parameter $\beta = 0.7$ taken from Fossati et al. (2012).

The distance from the cluster center can be approximated as the projected distance. Using positional angles of the galaxies (Yagi et al. 2010) and the cluster center (Bilton and Pimbblet 2018) we calculated the angular distance using spherical trigonometry

$$\cos(\Delta) = \sin(\delta_{\mathrm{G}})\sin(\delta_{\mathrm{C}}) + \cos(\delta_{\mathrm{G}})\cos(\delta_{\mathrm{C}})\cos(\alpha_{\mathrm{G}} - \alpha_{\mathrm{C}}). \tag{11}$$

Based on the distance from Earth to the cluster, Yagi et al. (2010) give the relation between the angle and the distance on the sky, where 1 arcsec corresponds to 473 pc. With angular distances $\Delta_{\mathrm{D100}} = 8'12''$ and $\Delta_{\mathrm{GMP2374}} = 18'44''$ we get the projected distance of the galaxies to the cluster center $r_{\mathrm{D100}} = 233\,\mathrm{kpc}$ and $r_{\mathrm{GMP2374}} = 532\,\mathrm{kpc}$.

This gives us ICM density at the location of D100 $\rho_{\mathrm{D100}} = 3.4 \times 10^{-27}\,\mathrm{g\,cm^{-3}}$ and at GMP2374 $\rho_{\mathrm{GMP2374}} = 1.1 \times 10^{-27}\,\mathrm{g\,cm^{-3}}$.

We calculated the radial velocities of the galaxies from their redshift by $v_{\mathrm{rad}} = c\,z$. We took values of redshift $z_{\mathrm{D100}} = 0.0177$, $z_{\mathrm{GMP2374}} = 0.0267$ from Yagi et al. (2010) and got velocities $v_{\mathrm{rad,D100}} = 5306\,\mathrm{km\,s^{-1}}$ and $v_{\mathrm{rad,GMP2374}} = 8004\,\mathrm{km\,s^{-1}}$. From these we subtracted the cluster radial velocity $v_{\mathrm{rad,Coma}} = 6995\,\mathrm{km\,s^{-1}}$ taken from Bilton and Pimbblet (2018) to obtain radial velocities relative to the cluster. To take into account the angular motion of the galaxies, we multiplied these values by a factor of $\sqrt{3}$. We obtained velocities $v_{\mathrm{D100}} = -2925\,\mathrm{km\,s^{-1}}$ and $v_{\mathrm{GMP2374}} = 1748\,\mathrm{km\,s^{-1}}$.

With the calculated values of ICM density and approximate velocity of galaxies relative to the cluster we determined the galaxies experience ICM pressure of $p_{\mathrm{ICM,D100}} = 2.9 \times 10^{-10}\,\mathrm{dyne/cm^2}$ and $p_{\mathrm{ICM,GMP2374}} = 3.4 \times 10^{-11}\,\mathrm{dyne/cm^2}$, where $1\,\mathrm{dyne}$ represents $1\,\mathrm{g\,cm\,s^{-2}}$.

5.4 Maximum ICM pressure estimate

According to Köppen et al. (2018), it is possible to approximate the maximum ICM pressure a galaxy has experienced during its orbit in the cluster. We can then compare this maximum pressure and the current pressure calculated in the previous subsection. When they are equal the galaxy is either before or near the pericenter of its orbit. If the maximum pressure is higher than the present pressure then the galaxy has probably already passed the peak of the pressure in the pericenter.

However, the model was defined with HI gas in mind. We assume the approximation is also suitable for molecular H_2. It is estimated from

$$p_{\max} = \frac{\Sigma_0}{\left[1 + (r_{\text{strip}}/R)^2\right]^{3/2}} \frac{v_{\text{rot}}^2}{g\, r_{\text{strip}}} \left[1 + a \exp\left(-\frac{r_{\text{strip}}}{R_0}\right)\right], \tag{12}$$

where Σ_0 denotes central gas surface density, r_{strip} is the radius at which matter is stripped from the galaxy, R is the radial scale for HI density, v_{rot} is the rotational velocity of the galaxy, g is the ratio of centrifugal force and maximum restoring force, $a = 15$ is a scaling factor and R_0 is the radial scale for the molecular gas fraction.

Carta is capable of reading astrometric data from the data cube, thus allowing us to measure distances in our images. Using first moment maps of our ALMA image cubes we determined the radii of the measured emission $r_{\text{strip,D100}} = 0.6\,\text{kpc}$ and $r_{\text{strip,GMP2374}} = 7.1\,\text{kpc}$.

According to the paper, the radial scales are related to the optical radius of the galaxy as $R = R_{\text{opt}}$ and $R_0 = \frac{2}{15} R_{\text{opt}}$. We took values of optical radii from Makarov et al. (2014) $R_{\text{opt,D100}} = 5.6\,\text{kpc}$ and $R_{\text{opt,GMP2374}} = 16.3\,\text{kpc}$.

To determine v_{rot} we opened the image cube in Carta and found the boundary channels (in units of $\text{km}\,\text{s}^{-1}$) in which we still see emission of the disk. Halving the difference of the two channels and correcting for inclination ($i_{\text{D100}} = 45°$, $i_{\text{GMP2374}} = 34.7°$ from Makarov et al. (2014)) we get $v_{\text{rot,D100}} = 131\,\text{km}\,\text{s}^{-1}$ and $v_{\text{rot,GMP2374}} = 246\,\text{km}\,\text{s}^{-1}$.

Using the value $g = 2$ as in the paper and an estimate of $\Sigma_0 = 10\,\text{M}_\odot\,\text{pc}^{-2}$ we get the peak pressure the galaxy has experienced $p_{\text{max,D100}} = 6.9 \times 10^{-10}\,\text{dyne/cm}^2$ and $p_{\text{max,GMP2374}} = 3.5 \times 10^{-11}\,\text{dyne/cm}^2$. Comparing these values and those from the previous subsection we can estimate the stage of the stripping process. For D100 the maximum pressure $p_{\text{max,D100}}$ is roughly 2.5 times bigger than the current $p_{\text{ICM,D100}}$. This could mean the galaxy is past the peak of the stripping force. Given the approximations we used this conclusion is uncertain. In the case of GMP2374, the stripping pressures have similar values meaning the galaxy is either yet to arrive into the peak or is currently at the peak of the stripping force. This is consistent with our previous conclusions based on the morphology of the galaxies, their gas content, as well as star formation activity.

Section 6:

Conclusions

We processed the interferometric data from the ALMA telescope and obtained images of the CO(2-1) emission, which is a tracer of the molecular gas component, in two jellyfish galaxies, D100 and GMP2374, that experience ram pressure stripping of their interstellar matter due to the interaction with the surrounding intra-cluster medium in the Coma cluster. We created moment maps of the image cube, which reveal the distribution of the emission, the velocity of the emitting matter and its velocity dispersion. We also produced position-velocity diagrams, which allow us to further analyze the distribution of velocity.

We found the galactic disk of the D100 galaxy has been heavily stripped of its gas component, that formed a long tail with a length of about 60 kpc. The distribution of the molecular gas in the tail is similar to the Hα measurements done by Yagi et al. (2010), but is concentrated in denser clumps. The radial velocity of the molecular gas in the tail increases with the distance from the galaxy center, which means it is being slowed relative to the cluster due to the interaction with the ICM. The velocity of the recently stripped gas, in the region just outside the galactic disk, exhibits an imprint of the rotation of the galactic disk, in the form of a velocity gradient perpendicular to the tail. We calculated the mass of the molecular gas component in the galactic disk and in the tail and found that the tail contains more than two times more molecular hydrogen than the disk.

The GMP2374 galaxy is far less disturbed by the interaction with the hot intra-cluster medium, although we still see some signs of asymmetry. There is a strongly stripped region between the galactic arms in the leading edge of the disk, and material is being stripped at the opposite side of the disk, in the form of unwinding spiral arms and a clump of gas south of the galaxy. A short tail behind the galaxy was revealed by weak emission of diffuse gas. The position-velocity diagram shows that the rotation of the disk also exhibits some deformation from the ram pressure. GMP2374 is clearly in an earlier, less effective stage of the stripping process than D100.

The difference in the stage of gas stripping in the two galaxies in the coherent environment of the Coma cluster is caused by different galactic properties, as well as different orbital parameters. These are key parameters that determine the efficiency of RPS, which consequently causes quenching of star formation and ultimately changes the morphological type of the galaxies, from blue, actively star-forming late types to red and passive early types.

References

Bilton, Lawrence E. and Kevin A. Pimbblet (Dec. 2018). "The kinematics of cluster galaxies via velocity dispersion profiles". In: MNRAS 481.2, pp. 1507–1521. DOI: 10.1093/mnras/sty2379. arXiv: 1808.10381 [astro-ph.GA].

Boselli, Alessandro, Matteo Fossati, and Ming Sun (Dec. 2022). "Ram pressure stripping in high-density environments". In: A&A Rev. 30.1, 3, p. 3. DOI: 10.1007/s00159-022-00140-3. arXiv: 2109.13614 [astro-ph.GA].

CASA Team and Associated Universities (2021). *CASA Documentation*. URL: https://casadocs.readthedocs.io.

Cavaliere, A. and R. Fusco-Femiano (Nov. 1978). "The Distribution of Hot Gas in Clusters of Galaxies". In: A&A 70, p. 677.

Cortes, Paulo et al. (Apr. 2023). *ALMA Cycle 10 Technical Handbook*. Additional contributors to this edition: Yoshiharu Asaki, Tim Bastian, Brian Mason, Crystal Brogan, John Carpenter, Chinshin Chang, Geoff Crew, Ed Fomalont, Misato Fukagawa, Remy Indebetouw, Hugo Messias, Todd Hunter, Ruediger Kneissl, Andy Lipnicky, Sergio Martin, Lynn Matthews, Luke Maud, Anna Miotello, Yusuke Miyamoto, Tony Mroczkowski, Hiroshi Nagai, Kouichiro Nakanishi, Masumi Shimojo, Richard Simon, Carmen Toribio, Catarina Ubach, Catherine Vlahakis, Martin Zwaan. DOI: 10.5281/zenodo.7822943. URL: https://doi.org/10.5281/zenodo.7822943.

Cortese, L., B. Catinella, and R. Smith (Aug. 2021). "The Dawes Review 9: The role of cold gas stripping on the star formation quenching of satellite galaxies". In: PASA 38, e035, e035. DOI: 10.1017/pasa.2021.18. arXiv: 2104.02193 [astro-ph.GA].

Fossati, Matteo et al. (Aug. 2012). "65 kpc of ionized gas trailing behind NGC 4848 during its first crossing of the Coma cluster". In: A&A 544, A128, A128. DOI: 10.1051/0004-6361/201219933. arXiv: 1207.4806 [astro-ph.CO].

Gunn, James E. and III Gott J. Richard (Aug. 1972). "On the Infall of Matter Into Clusters of Galaxies and Some Effects on Their Evolution". In: ApJ 176, p. 1. DOI: 10.1086/151605.

Högbom, J. A. (June 1974). "Aperture Synthesis with a Non-Regular Distribution of Interferometer Baselines". In: A&AS 15, p. 417.

Hubble, Edwin (1937). "The Realm of the Nebulae". In: *Ciel et Terre* 53, p. 194.

Jáchym, Pavel et al. (Apr. 2017). "Molecular Gas Dominated 50 kpc Ram Pressure Stripped Tail of the Coma Galaxy D100". In: ApJ 839.2, 114, p. 114. DOI: 10.3847/1538-4357/aa6af5. arXiv: 1704.00824 [astro-ph.GA].

Köppen, J. et al. (Oct. 2018). "Ram pressure stripping made easy: an analytical approach". In: MNRAS 479.4, pp. 4367–4390. DOI: 10.1093/mnras/sty1610. arXiv: 1806.05887 [astro-ph.GA].

Makarov, D. et al. (Oct. 2014). "HyperLEDA. III. The catalogue of extragalactic distances". In: A&A 570, A13, A13. DOI: 10.1051/0004-6361/201423496.

Marr, Jonathan M, Ronald L Snell, and Stanley E Kurtz (2015). *Fundamentals of radio astronomy: observational methods*. Vol. 13. CRC Press.

McMullin, J. P. et al. (Oct. 2007). "CASA Architecture and Applications". In: *Astronomical Data Analysis Software and Systems XVI*. Ed. by R. A. Shaw, F. Hill, and D. J. Bell. Vol. 376. Astronomical Society of the Pacific Conference Series, p. 127.

Sanders, J. S. et al. (Jan. 2020). "Measuring bulk flows of the intracluster medium in the Perseus and Coma galaxy clusters using XMM-Newton". In: A&A 633, A42, A42. DOI: 10.1051/0004-6361/201936468. arXiv: 1911.13108 [astro-ph.CO].

Schawinski, Kevin et al. (May 2014). "The green valley is a red herring: Galaxy Zoo reveals two evolutionary pathways towards quenching of star formation in early- and late-type galaxies". In: MNRAS 440.1, pp. 889–907. DOI: 10.1093/mnras/stu327. arXiv: 1402.4814 [astro-ph.GA].

Solomon, P. M. and P. A. Vanden Bout (Sept. 2005). "Molecular Gas at High Redshift". In: ARA&A 43.1, pp. 677–725. DOI: 10.1146/annurev.astro.43.051804.102221. arXiv: astro-ph/0508481 [astro-ph].

Yagi, Masafumi et al. (Dec. 2010). "A Dozen New Galaxies Caught in the Act: Gas Stripping and Extended Emission Line Regions in the Coma Cluster". In: AJ 140.6, pp. 1814–1829. DOI: 10.1088/0004-6256/140/6/1814. arXiv: 1005.3874 [astro-ph.CO].